

Evaluation of CFD for Simulation of High-Supersonic Control-Surface Effectiveness

James C. Ross¹, Marie F. Denison², Robert E. Childs³, Joseph A. Garcia⁴, Paul M. Stremel⁵,
Veronica M. Hawke⁶, Hannah R. Spooner⁷
NASA Ames Research Center, Moffett Field, CA, 94035, USA

Matthew A. Reed⁸, Bil L. Kleb⁹, Anthony N. Watkins¹⁰, Paul M. Danehy¹¹, Ross A. Burns¹²,
Timothy W. Fahringer¹³, Stephen E. Borg¹⁴

NASA Langley Research Center, Hampton, VA, 23681, USA

Philip E. Robinson¹⁵
NASA Johnson Space Center, Houston, TX, 77058, USA

As part of studying the ability of Computational Fluid Dynamics (CFD) to accurately model important flow physics in the high-supersonic Mach number range, control-surface effectiveness on an entry vehicle for Mars exploration was examined. As with several other important flow regimes studied under the CFD as Surrogate for Wind Tunnel Testing at High Supersonic Speeds Project, a combined CFD and wind-tunnel study of a proposed Mars landing configuration was undertaken. The testing was performed in high-speed test section of the NASA Langley Research Center's Unitary Plan Wind Tunnel. The CFD team was an integral part of the overall evaluation team throughout the model development and test planning process and performed pre-test computations predicting the results of the testing. For the CFD predictions of the model in the wind tunnel, the flow into the test section was imposed as a boundary condition. The imposed inflow was based on a previous flow characterization study and companion CFD simulating the flow from the settling chamber through the test section. This paper presents a description of the testing and the resulting aerodynamic data. A summary of comparisons of the experimental and CFD results will also be presented as well as a cost comparison of the two approaches to generate data on this previously untested vehicle shape.

¹ Aerospace Engineer, Experimental Aerophysics Branch, AIAA Associate Fellow.

² Research Engineer, NASA Advanced Supercomputing Division, AIAA Member.

³ Research Engineer, Science and Technology Corporation, AIAA Member.

⁴ Research Engineer, Systems Analysis Office, AIAA Member.

⁵ Research Engineer, Science and Technology Corporation, AIAA Member.

⁶ Research Engineer, Science and Technology Corporation, AIAA Member.

⁷ Instrumentation Engineer, Wind Tunnel Systems Branch.

⁸ Test Engineer, Jacobs Technology Inc., Member AIAA.

⁹ Senior Researcher, Aerothermodynamics Branch, AIAA Associate Fellow.

¹⁰ Research AST, Advanced Measurements and Data Systems Branch, AIAA Senior Member.

¹¹ Senior Researcher, Advanced Measurements and Data Systems Branch, AIAA Associate Fellow.

¹² Research Engineer, National Institute of Aerospace.

¹³ Lead Researcher AST, Advanced Measurements and Data Systems Branch, AIAA Member.

¹⁴ Research AST, Advanced Measurements and Data Systems Branch, AIAA Senior Member.

¹⁵ Research Engineer, EG-311.

I. Nomenclature

α	= angle of attack, deg.
β	= yaw angle, deg.
σ	= measurement uncertainty, 1 standard deviation
S_{ref}	= model reference area
L_{ref}	= model reference length
C_p	= pressure coefficient
CA	= force coefficient in the model axial direction
CN	= force coefficient in the model normal direction
CY	= force coefficient in the model lateral direction
$CMCG$	= pitching-moment coefficient at the vehicle center of gravity
$CYMCG$	= yawing-moment coefficient at the vehicle center of gravity
$CRMCG$	= rolling-moment coefficient at the vehicle center of gravity
$CHMFL$	= left-hand flap hinge moment coefficient
$CHMFR$	= right-hand flap hinge moment coefficient
$CHMFLminusR$	= difference between left-flap and right-flap hinge-moment coefficient
δF	= left-hand flap deflection angle, degrees
M	= Mach number
Re	= unit Reynolds number, Million/foot
AF	= axial force measured by the internal balance
NF	= normal force measured by the internal balance
SF	= side force measured by the internal balance
X	= axial coordinate in streamwise direction from start of test section, inches
Xm	= axial location of model nose
Y	= lateral coordinate in test section
Z	= vertical coordinate in test section
Subscripts	
L	= left
R	= right
cg	= center of gravity

II. Introduction

In 2012, the Unitary Plan Wind Tunnel at NASA's Langley Research Center was placed on the demolition list with a target date of 2022. Since then, the facility has been mothballed for several months, operated by Jacobs Engineering Group under a full-cost recovery model with no investment in upgrades or improvements. The tunnel was eventually reopened as a NASA facility to perform aerodynamic testing for the Space Launch System. It remains on the demolition list for 2022, however, despite a recent increase in demand for testing in the facility. This study of the ability of Computational Fluid Dynamics (CFD) to predict the control effectiveness for high-supersonic flight is one of six such evaluations covering a wide range of flow physics and vehicle types. Before the facility is permanently closed and demolished, NASA's Mission Support Council asked the Aerosciences Evaluation and Testing Capability (AETC) Management to perform the overall CFD Evaluation Project to identify any technical risks to NASA and national programs that might result from relying solely on CFD for aerodynamic data in the Mach 2.4 to 4.6 range.

In addition to the technical risks, the potential fiscal risks of eliminating a facility in favor of computational simulations need to be addressed. The cost associated with generating a database solely from CFD needs to be estimated to ensure that if the facility is closed, there are enough experienced CFD practitioners and computational resources available to take up the full workload of the wind tunnel every year.

A. Results Comparison Ground Rules

The first ground rule for the CFD Evaluation Project [1] is that the CFD effort must be staffed and funded by a partner project while AETC funds the testing activities. This ensured that the results generated serve more than the purpose of evaluating the accuracy and cost of CFD relative to the wind tunnel. In the current study, the interested partner project Game Changing Development Program which, among other topics, is studying new ways to deliver payloads to Mars. The configuration chose for the study is the Co-Optimization Blunt-body Re-entry Analysis Mid-L/D Rigid Vehicle (CobraMRV) [2]. This vehicle is designed to deliver large payloads to the surface of Mars

through a standard entry and descent down to a Mach number of around 2. At this point further deceleration is provided by a retro-propulsion system which is used during the remainder of the descent down to a soft landing. Figure 1 shows the conceptual entry, descent, and landing for the vehicle. This paper describes the evaluation process, testing, test results, and some comparisons between the wind-tunnel and CFD results appropriate to the unpowered descent from approximately Mach 4.6 down to 2.4. A companion paper describes the CFD methods employed and details of the simulations [3].

The comparisons between results from CFD and experimental data were primarily for the model forces and moments. In this paper those will be reported in body axes with the nominal vehicle center of gravity as the moment reference point. The experimental measurement uncertainty due to the balance and dynamic pressure uncertainties were the largest contributors and are the only sources included here. A full uncertainty analysis will be done for the final report. Pressure distributions obtained using pressure sensitive paint (PSP) were useful to understand the differences seen between the CFD and experimental results and to help explain unexpected results from the wind-tunnel test.

Each of the Evaluation Teams was required to define the geometry of the wind-tunnel model and use that geometry for model fabrication and to simulate the eventual test in the wind tunnel. These pre-test predictions are the results that were eventually used in the CFD/WT comparisons. These were called pre-test predictions in spite of not being fully complete before the testing started. The experimental data, however, was not made available outside the testing team until all the pre-test predictions were complete. The intent was to ensure that the CFD was done using best practices generated by the CFD team without access to the wind-tunnel data, much like would be the case if the wind tunnel was not available. In this evaluation, two CFD codes were employed in the predictions: OVERFLOW [4] and FUN3D [5]. After the comparisons with the wind-tunnel data, the plan is to have a second round of computations with the focus on finding and correcting any deficiencies in the pre-test predictions. This step is intended to differentiate between errors in the choice of best practices by which the pre-test predictions were computed and a possible deficiency in the ability of a particular code to properly predict the force and moments generated by the model in the test section.

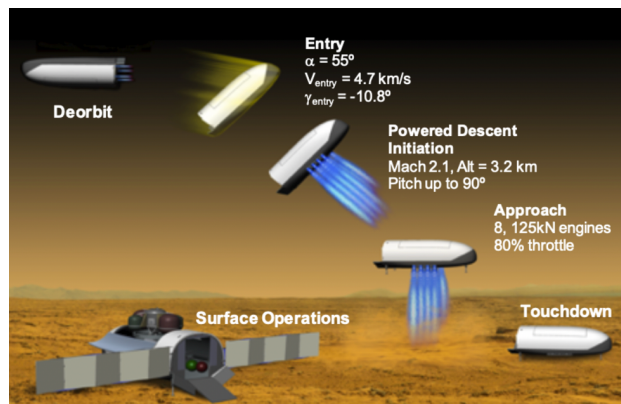


Fig. 1 CobraMRV concept showing the proposed entry, unpowered and powered descent, and landing on Mars.

B. Cost Comparisons

The cost of obtaining data through wind-tunnel testing and CFD were also compared. The comparison is intended to cover tests that are used to generate an aerodynamic database as well as tests used to understand flow physics or to evaluate CFD results. A typical database test will cover many configurations and flow conditions. In this wind tunnel, for a given test condition (configuration and flow), a run would consist of a sweep through the angle-of-attack range. This is usually repeated for several sideslip conditions before moving on to another flow condition. The number of angles of attack at which data are acquired can range from 10 during a pitch-pause data acquisition process to over 1,000 during a continuous-sweep process. This is a very efficient data collection process once the model is designed, built, installed in the test section, and all the instrumentation hooked up and verified.

For generating a database with CFD, the process is a bit different. Starting with the geometry definition, the next step is to turn it into computational grids. This usually involves first updating the geometry to make it watertight and suitable for grid generation. This can take hours to a week or more depending on the complexity of the model and the state of the geometry definition. Grid generation itself is an automated process but a new grid, or portions of grid, are required for every model configuration. The solutions at a given flow condition can be relatively expensive,

depending on the character of the flow generated, e.g., substantially attached, separated, or separated and reattaching. Separated flows can vary in difficulty depending on whether it is from a sharp edge or on a smooth surface. At any rate, the incremental cost of a CFD solution can be much larger than that for experimental data. The preparation time and expense are likely to be much smaller than for a wind-tunnel test. The comparisons sought in this program are intended to capture all of the costs for both the experiment and CFD and interpret them in the context of the two general types of studies described above.

III. Wind-Tunnel Test Description

A. Wind Tunnel Description

The Unitary Plan Wind Tunnel at NASA's Langley Research Center (LUPWT) is a closed circuit, continuous flow, variable-density supersonic wind tunnel. It has two test sections that measure approximately 4 by 4 by 7 feet. The test described here was performed in the high-speed test section that has a Mach-number range of 2.3 to 4.6. By varying the total pressure tests can be performed at unit Reynolds number from approximately 0.5 to 8.25 million per foot. A complete description of the facility can be found in reference 6.

Figure 2 shows a side view of the nozzle through the test section of the high-speed leg of the LUPWT. The Mach number in the tunnel is primarily controlled by setting the lower nozzle block axial location. Because of the nozzle asymmetry, the flow in the test section is slightly asymmetric in the vertical direction. To account for this flow asymmetry, a flow characterization test was performed with companion CFD analyses [7]. That work was one of the evaluation cases for the overall CFD Evaluation Project [1]. Data was acquired for the CFD comparisons at Mach number combinations of $M \approx 2.4$, $Re = 3$ M/ft; $M \approx 3.5$, $Re = 1, 3, \& 4.5$ M/ft; and $M \approx 4.6$, $Re = 1, 3, \& 4.5$ M/ft.

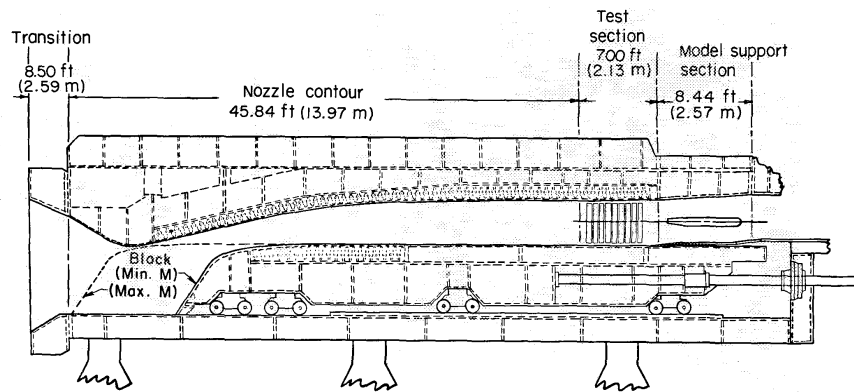


Fig. 2 Side view of high-speed test section of the LUPWT [4].

B. Model Configuration

Figure 3 shows the overall CobraMRV configuration and the control surfaces that are the focus of this work. The model scale is approximately 2% and the resulting dimensions are shown in the Figure. A short section of each tail surface is fixed and doesn't rotate with the rest of the flap. This became a convenient surface for attaching the flaps to the model. The fixed portions of the flaps were made into parts of a pair of moment gages which provided hinge moments on both flaps. There were 11 flaps manufactured for each side of the model, covering a range of deflection angles from -35° to $+35^\circ$, which was needed for the aerodynamic database. Figure 3 shows the range of deflection angles and the attachment to the hinge-moment gage. There was a small 0.020" gap between the flap elements that provided a leak path from the pressure side to the suction side of the flaps between the two beams of hinge-moment gages. This was judged to be a small enough gap so as not to affect comparisons with CFD results not containing the gap. This was borne out by computations that modeled the actual geometry and a geometry with the gap sealed that showed no differences in the pressures more than a few gap thicknesses away from the gap.

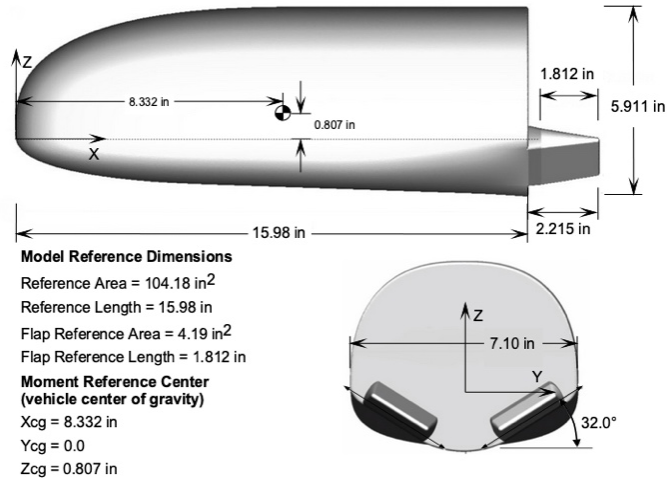


Fig. 3 CobraMRV wind-tunnel model showing overall and reference dimensions.

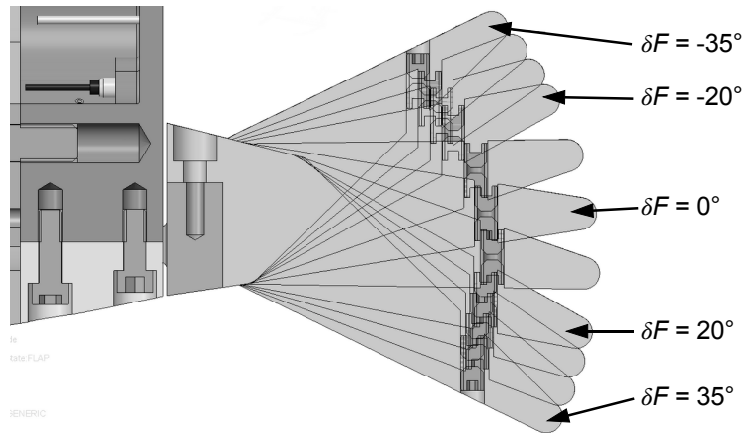


Fig. 4 Composite view showing the left-hand flaps the model. An identical set was made for the right side of the model. The flaps are each bolted to a hinge-moment balance.

Table 1 shows the flap angles and the combinations that were tested. Four of the configurations included the full instrumentation suite for the aerodynamic measurements for comparison with the CFD results. In addition, the more limited data acquired (no PSP) for configuration 13 was also used for the CFD comparisons. The flap deflection combinations chosen for the CFD/WT comparisons cover the full range of flow types generated by the flaps. With the given range of flap deflections, the flow on the pressure side of the flaps and immediately upstream include fully attached flow (zero flap deflection), three-dimensional compression-corner separation and reattachment (positive flap deflection, and sharp-corner separation (negative flap deflection). When deflected symmetrically, the flaps produce pitch control. When they are deflected asymmetrically, they produce very little body-axis roll but significant body-axis yawing moment. The selected deflection combinations cover both types of control inputs.

The model was fabricated using standard machining typical of wind tunnel models. The back shell and nose are made of aluminum while the heat shield was made of stainless steel. The stainless-steel material chosen for a separate wind-tunnel test investigation looking at the effect of locally elevated surface temperature on the boundary-layer behavior. The balance block and other internal structure was also machined from stainless steel as was the custom sting.

Table 1. Model flap angles and the combinations used during the wind-tunnel testing. The lightly shaded cells indicate their use only for the database while the black cells provided more detailed data for the CFD comparisons. The numbers in the colored cells are the assigned configuration numbers.

Left Flap	Right Flap								
	-35°	-30°	-20°	-10°	0°	10°	20°	30°	35°
-35°	16								
-30°									
-20°			14						
-10°		13		11		7			
0°					1				
10°				5		6			
20°			9		8		2		
30°						3			
35°									4
	Evaluation		Database						

C. Model

The model is mounted on an internal balance attached to a bent sting that penetrates the model back shell near the aft end. There is a small gap around the sting visible in Figure 5. Since all the joints between model parts were tightly sealed to prevent leakage, this detail was also deemed to be small enough to omit from the CFD. The nominal angle of attack for the vehicle during descent is 55° with a range of interest for the aerodynamic database of 40° to ~100°. This would cover the entire entry and descent flight including the transition to 90° angle of attack before starting the retro-propulsion rockets at around Mach 2. The model support system in the wind tunnel is limited to a maximum of 29° of motion. Centering the range around the desired trim angle put the angle of attack range at 41° to 70°. The photo in Figure 4 shows the model at 55° angle of attack.

Installation



Fig. 5 Photograph of the model in the wind tunnel.

D. Instrumentation

The primary data for comparison with CFD was force and moment coefficients for the overall model and the flap hinge moments. The LRC-716-1K-1.5A balance was chosen for this test for its close match to the maximum aerodynamic loads for the model at the chosen test conditions. Custom hinge moment balances were procured with the appropriate load range. The flap mounting block on the gages were shaped to match the fixed part of the flaps on the CobraMRV. The model angle of attack was measured using a precision accelerometer.

The surface pressure distribution was also important to help understand any potential differences between the CFD and WT results. 60 pressure taps were installed in rings around the model at seven axial stations with between one and nine taps per ring. There was some concern that the flow on the leeward-side of the model might be unsteady, so three high-rate pressure transducers were installed on the upper/aft section of the back shell and three more on the rear face of the model. The layout of the static taps and unsteady pressure transducers are shown in Figure 6.

No correction due to the cavity pressure was made to the wind-tunnel data. The CFD-generated forces and moments did not include any contributions from the area of the sting cutout on the model, although the sting gap was not present in the CFD geometry.

The model was coated with PSP to obtain detailed pressure distributions. The static pressure taps provided local anchoring of the PSP results to known pressures. This reduced the effect of varying temperature on the PSP measurements as the PSP did not have temperature compensation. Cameras and lighting were arranged on both windows of the test section to provide pressure measurements on all surfaces of the model. Priority was given to the lower surface of the model (pressure side facing the oncoming flow) to observe the flow on that side of the flaps.

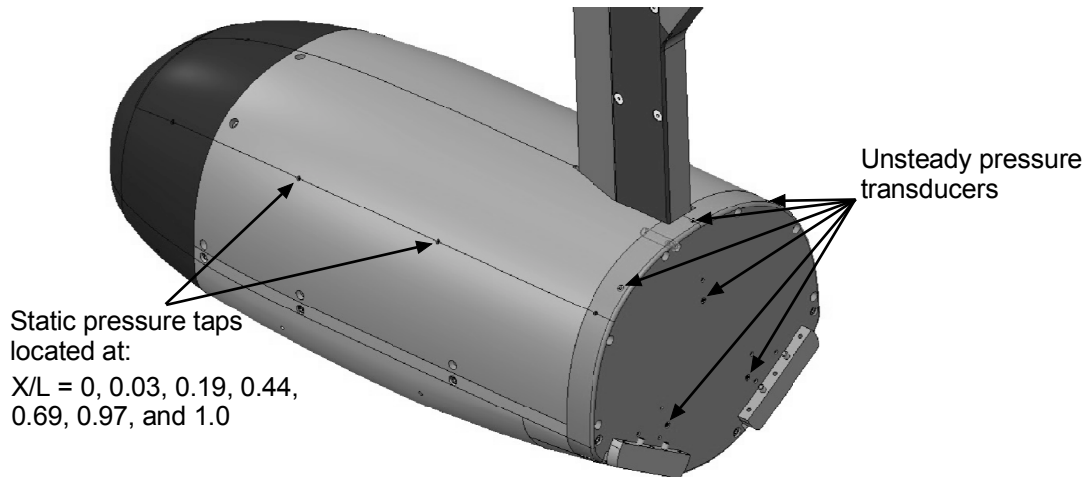


Fig. 6 Locations of the static pressure tap rings and unsteady pressure transducers. Mounting surfaces on the hinge-moment gages are shown without the flaps attached.

A secondary comparison between the CFD results and experimental data will be the flow field in the vicinity of the impingement of the model bow shock on the floor of the wind tunnel. Shock-boundary-layer interactions are a difficult flow to simulate in CFD, so this was an opportunity to make comparisons between wind-tunnel data and CFD predictions in a very different flow than perhaps has been done before. Our original intent was to use Pulse-burst, cross-correlation Doppler global velocimetry (PB-CC-DGV) [8] to measure the flow near the model in the area upstream of and below one of the body flaps on the model. The plan was to use natural seeding generated by introducing humidity into the wind tunnel and the resulting ice crystals that form as the humid air passes through the wind-tunnel nozzle, rapidly dropping the temperature. The ice crystals made very good particles for the DGV but unfortunately did not persist as ice crystals far enough downstream of the model bow shock to be used to measure the flow on the high-pressure side of the flaps. Measuring the flow in the shock/floor boundary layer interaction region was an excellent second choice as the ice crystals persisted long enough to document this region of the flow.

PB-CC-DGV is a velocimetry technique using a pulse-burst laser in combination with high-speed imaging. The flow velocity is measured by the Doppler shifts relative to a zero-velocity reference. High-speed planar laser Mie scattering (PLMS) is a flow visualization technique that images laser light scattered from small particles in the flow (ice crystals in this case) and allows for the visualization of the mean flow structures (e.g., bow shock) and unsteady features (e.g., vortices, incipient separation bubbles). The measurements captured roughly half of the tunnel cross-sectional area and focused on the shock-boundary layer interaction beneath the model. Additionally, axially scanning the COBRA model allowed the stationary measurement plane to capture pseudo-tomographic information. Figure 7 shows several flow-visualization images from the DGV system. The laser sheet is located at six X-stations relative to the model roughly corresponding to slightly upstream of the flaps (44 in.), near the flap-body junction (42 in.), over the flaps (41 in.), near the flap trailing edges (40 in.), and downstream of the flaps (39 and 37 in.). The shocks generated by the flaps are clearly visible at 41 and 40. At $X_m = 39$ and 37 inches, the flap shocks are harder to discern as they are interacting with the main model shock. Other images show the spatial evolution of both the

bow-shock structure and that of the shock-boundary layer interaction. The comparisons between the measured and predicted flow fields have not been done yet. The comparisons will be included in subsequent publications.

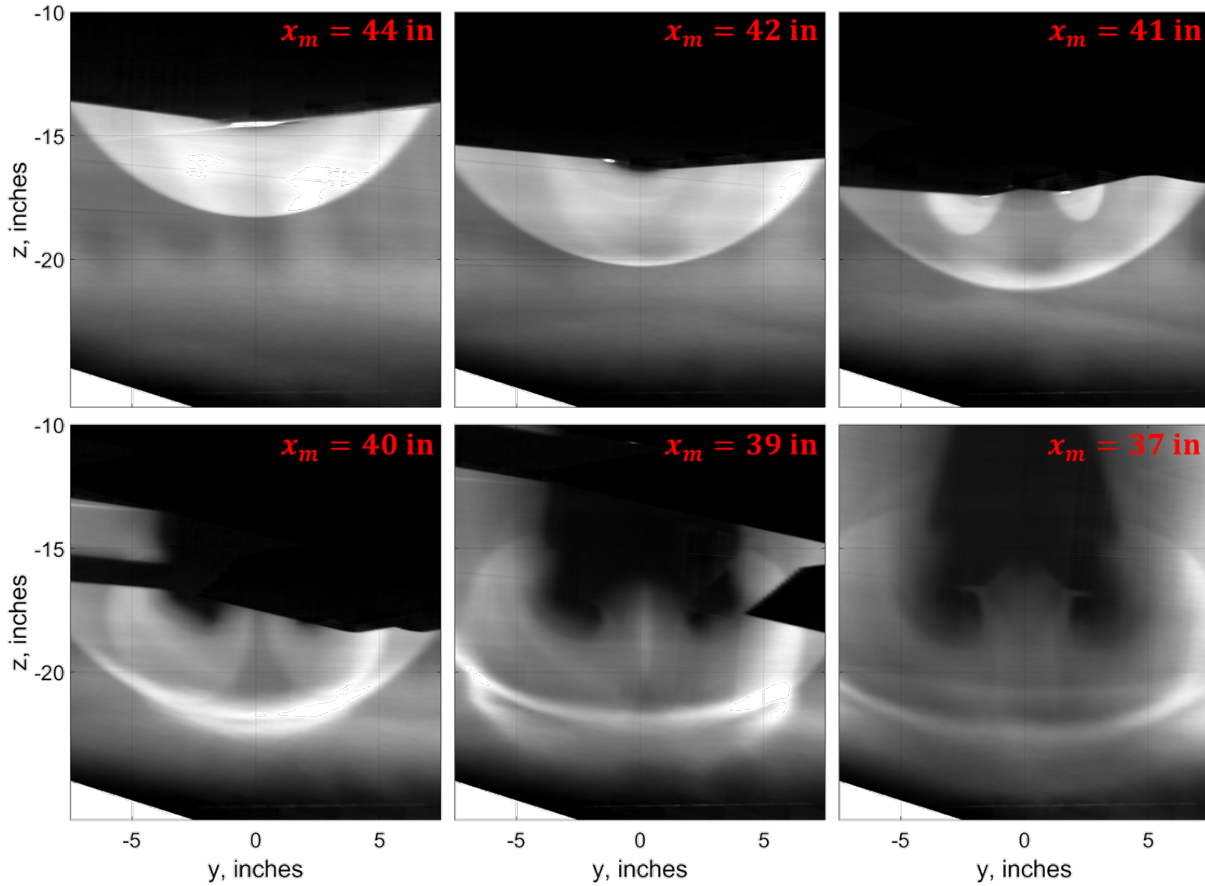


Fig. 7 Off-body flow visualization showing the spatial evolution of the bow-shock/boundary layer interaction. Model position is indicated in each frame. Images were taken with symmetric flap deflections, $\delta F_L = \delta F_R = 35^\circ$, at Mach 3.5, Re 3 M/ft, $\alpha = 41^\circ$, $\beta = 0^\circ$.

E. Effect of boundary-layer tripping

An important aspect of the testing was to ensure that the boundary layer on the lower surface of the model was turbulent. That will likely be the state of the boundary layer for the actual vehicle at the Mach numbers we tested the model at. More importantly, the boundary layer was expected to be transitional across the range of conditions, so a trip strip was applied to the heat-shield side of the model at the location where transition was predicted in preliminary CFD. The location of the trip strip, which consisted of individually bonded grains of sanded, sifted to have a nominal size of 0.047". The trip strip is shown in Figure 8 superimposed on an image of the CFD solution. The color contours show the local pressure coefficient, and the surface streamlines are also shown. The grit was applied in an arc, so the trip strip was approximately perpendicular to the local flow direction. The effect of the grit on the aerodynamic forces and moments was small but measurable, so the grit was in place during the entire test.

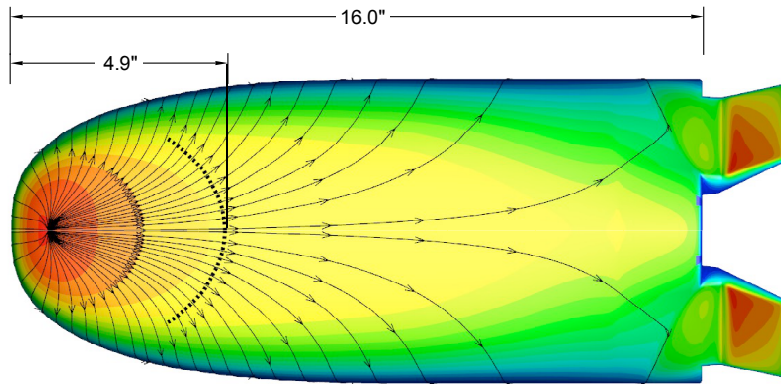


Fig. 8 Computed pressure coefficient contours and surface streamlines (OVERFLOW) with the trip grit shown at the location it was bonded to the model in the wind tunnel. Mach number = 2.4, Re 1 M/ft.

F. Infra-Red Imagery

IR imagery was used primarily to check the boundary-layer state on the heat-shield side of the model at the test conditions used for CFD evaluation. To make these images, the model was rolled 90° to orient it with the heat shield facing the side wall of the wind tunnel, in which a small IR-transmitting window allowed imaging of the model heat shield. For these images, the model had previously been painted black to reduce flair from the model surface during the DGV measurements. Figure 9 shows a representative IR image at M 3.5 and Re 3 M/ft.

The aerodynamic changes measured with and without the grit indicated a measurable but small change in the axial force and flap hinge moments. Therefore, the grit was left on the model for the duration of the test.



Fig. 9 Infra-red image of the model surface showing transition occurring at or before the grit elements. Mach number 3.48, Re 3 M/ft.

IV. Experimental Uncertainty

By far, the largest contributors to the force and moment measurement uncertainty were the balance residuals and uncertainty in the dynamic pressure. The uncertainty in the aerodynamic coefficients were computed for every data point [9]. One experimental uncertainty source that was difficult to quantify was the effect of model position on the force and moment measurements. This uncertainty source has been identified previously by Rhode, et al [10], but requires a large number of repeat runs at different model locations, preferably in all three directions. Instead, this uncertainty will be determined using CFD following the process defined by Baurle [11] and included in the final report.

V. CFD Analyses

Following the ground rules of the evaluations, two CFD codes were used to perform the predictions prior to releasing the wind-tunnel data. OVERFLOW [4] and FUN3D [5] were chosen for this evaluation. OVERFLOW is a well-established CFD code developed by NASA over several decades. It was chosen as one of the codes for this study based on its long history of use with NASA and that it employs structured, overset grids and is relatively efficient in computer usage. Figure 10 shows the surface grids that were used in OVERFLOW for the model, model support and wind tunnel floor. The sidewalls and outflow boundary are not shown in this rendering.

The second code selected for the study is FUN3D, another well-established and heavily used code, which was chosen for its use of unstructured, adaptive meshing and it is also heavily used within NASA. Figure 11 shows a typical solution for the COBRAMRV configuration at Mach 2.4, Re 3 M/ft, and 55° angle of attack. The grid adaption to the rapid density changes at the shocks and expansions is readily apparent as is the interaction of the bow shock and the wind-tunnel floor boundary layer.

Analyses were performed with the full model support and with only the sting and roll mechanism using FUN3D and showed little difference. All the OVERFLOW solutions include the full model support system while the FUN3D solutions only included the model, sting, and roll mechanism. Full details of the CFD performed as part of this evaluation are given in Reference [3].

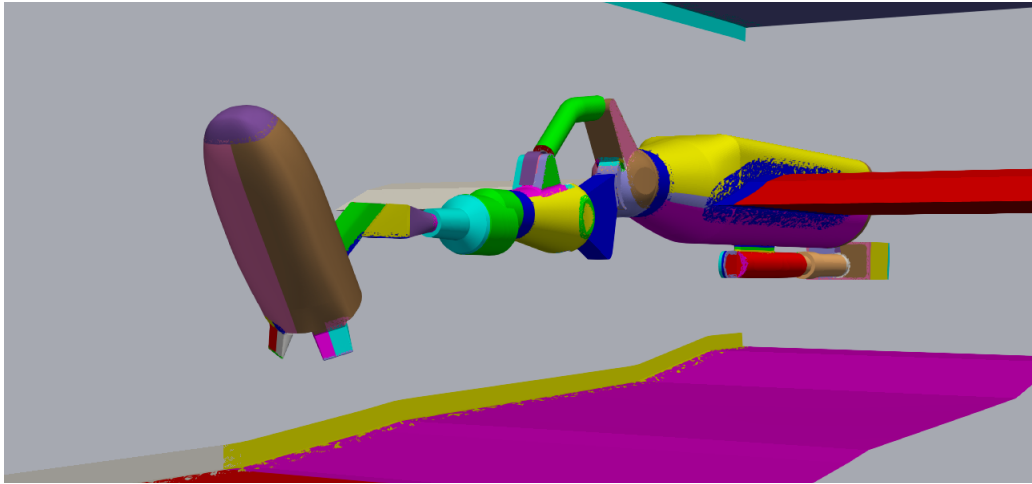


Fig. 10 Structured, overset grid system used for the OVERFLOW analyses.

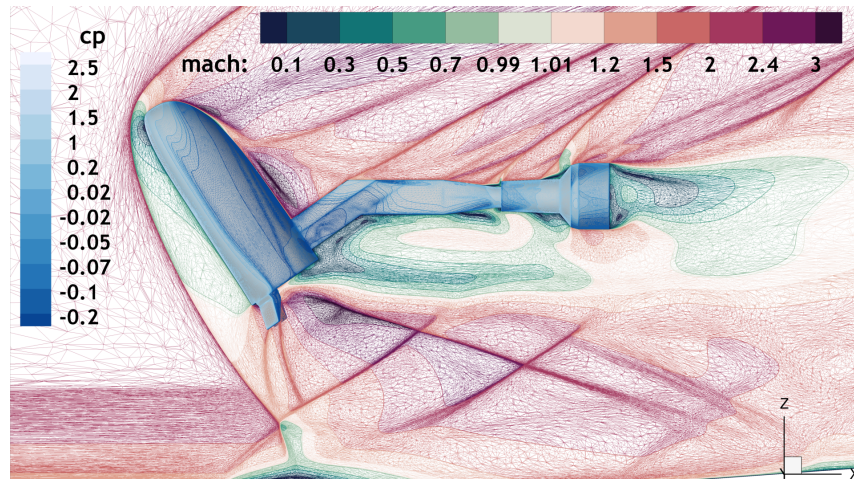


Figure 11 Example of FUN3D solution and adaptive mesh used in the CFD evaluation. $M = 2.4$, $Re = 3 \text{ M/ft}$, $\delta F_L = \delta F_R = 20^\circ$.

VI. Results and Initial Comparisons

The primary interest was comparisons between the computed and measured forces and moments generated by the model in the wind tunnel. All six aerodynamic forces and moments plus the left and right flap normal-force and hinge-moment coefficients were compared at 35 test conditions that spanned the range of all the test parameters. Typically, this included three angles of attack for a particular flap deflection combination at a given sideslip angle, Mach number, and Reynolds number. For some Mach- and Reynolds-number combinations, results at only one or two angles of attack were compared.

A. Force and Moment Coefficient Comparisons

A typical comparison of the force and moment is shown in Figure 12. In this case the flap deflections were both 20° , the sideslip angle is 0° , $M = 3.48$, and $Re = 1 \text{ M/ft}$. The measurement uncertainty due only to balance and dynamic-pressure uncertainty shown as $\pm 2\sigma$ bars on the data points acquired during the PSP data acquisition. As an indication of the near-term repeatability of the data, the results of a continuous-sweep run, which were usually run back-to-back, are also shown. Figure 13 shows a similar comparison of the flap hinge moments for the same test condition. The data points denoted by the solid blue circles are the time-averaged points acquired along with the PSP pressure distributions. These points also have the experimental uncertainty noted by $\pm 2\sigma$ bars. The FUN3D predicted values are shown as red squares while the OVERFLOW predictions are shown as black diamonds.

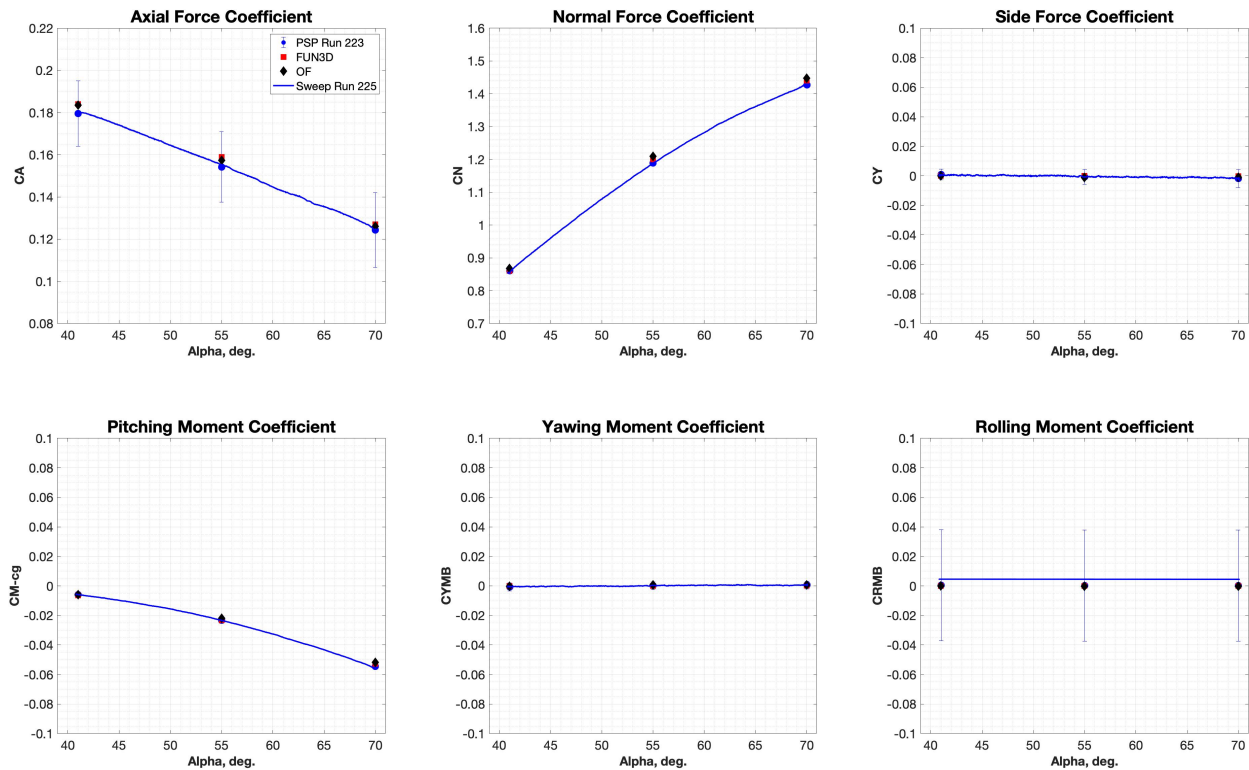


Fig. 12 Comparison of predicted and measured body-axis aerodynamic coefficients for the COBRAMRV model. Configuration 2 ($\delta F_L = \delta F_R = 20^\circ$) $M = 3.48$, $Re = 1 \text{ M/ft}$, and $\beta = 0^\circ$. Uncertainty bars represent the $\pm 2\sigma$ uncertainty due to the balance and dynamic pressure measurement uncertainties.

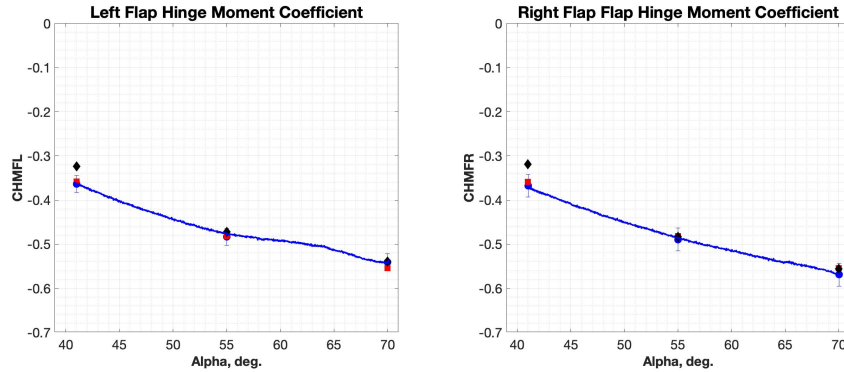


Fig. 13 Comparison of predicted and measured aerodynamic coefficients for the CobraMRV model. Configuration 2 ($\delta F_L = \delta F_R = 20^\circ$) $M = 3.5$, $Re = 1$ M/ft, $\beta = 0^\circ$.

For most of the comparisons, the uncertainty bars are small, making it difficult to tell visually if the predictions are within the measurement uncertainty. The difference between the predicted and measured was determined and the predicted coefficients that were within 2σ of the measured value are called good. Requiring the predicted aerodynamic coefficients to be within this uncertainty of the experimental data is strict, but the full CFD uncertainty quantification has not been completed yet. This is probably a stricter criterion than it will prove to be with the full uncertainty analysis. The full analysis will also allow an estimate of the model-form errors and will be included in the final report for the project.

B. Quantitative Comparison with CFD Predictions

Table 2 shows a small section of the spreadsheet used to evaluate the overall accuracy of the CFD predictions for all the cases in the comparison. Two blocks of the force and moment coefficients are shown summarizing the results for two test conditions at the three angles of attack used for the comparisons. The table shows the configuration number, Mach number, Reynolds number, and sideslip angle along with the corresponding run numbers from the experiment. Each of the force and moment coefficients are noted with the differences between the predicted and measured values as multiples of the 1σ experimental uncertainties for each coefficient in the six right-hand columns of the table.

Good agreement is noted by the unshaded background for an entry while a shaded entry indicates that the prediction was more than 2σ from the experimental value. Not surprisingly, the lower-Re test conditions were predicted well more often than the higher-Re conditions. The aerodynamic coefficient uncertainty for the low-Re cases is higher so the predicted values can be further from the nominal and still count as good. Another trend was that the predictions were better for flap deflections less than 35° , including asymmetric flap deflections. For the 35° symmetric flap deflection case, the force and moment coefficients were predicted accurately less than 50% of the time, even at the low-Re test conditions. Sideslip angle seemed to have no significant effect on the accuracy of the predictions. The predictions for -35° symmetric flap deflections were significantly better than average with $\sim 70\%$ within 2σ of the experimental value (but with a smaller sample size and only FUN3D predictions).

Another interesting feature of the comparisons is the large range of the mismatches between CFD predictions and wind-tunnel measurements. The differences in terms of multiples of the measurement standard deviations range from zero to as high as 81 for the first test condition. This is not typical, but 9% of the predicted coefficients are off by 10σ or more and 3% are off by more than 20σ . Overall, 60% of the OVERFLOW predicted force and moment coefficients and 58% of the FUN3D predictions are within $\pm 2\sigma$ of the experimental values. This mediocre agreement does not seem good enough to rely solely on CFD with no wind-tunnel data in this Mach number range.

Table 2. Rating the predicted force and moment coefficients from OVERFLOW and FUN3D at 2 test conditions for configuration 1 ($\delta F_L = \delta F_R = 0$): M 2.40, Re 3 M/ft, $\beta = 0^\circ$; and M 3.48, Re 1 M/ft, $\beta = 0^\circ$.

Config.	Mach	Re, M/ft	Beta	Run Numbers PSP	Run Numbers Database	Aero Coefficient	Difference - multiples of sigma					
							Overflow			FUN3D		
							41°	55°	70°	41°	55°	70°
1	2.399	3.0	0.0	170	138	CA	1.5	0.6	1.5	3.2	1.3	3.5
						CN	9.0	10.0	66.5	21.8	17.6	81.2
						CY	0.9	0.0	1.1	11.4	0.1	0.4
						CMCG	7.4	0.9	37.3	11.2	6.5	24.7
						CYMB	2.6	0.6	8.6	1.1	1.1	1.8
						CRMB	0.1	0.1	0.1	1.0	1.0	0.9
						CHMFL	4.3	1.4	2.9	12.7	6.5	4.1
						CHMFR	5.1	4.7	13.2	3.5	0.1	12.8
						CHMFLminusR						4.1
1	3.477	1.0	0.0	156, 161	155	CA	0.5	0.3	0.4	0.5	0.7	0.7
						CN	2.8	5.9	6.7	0.3	2.8	5.7
						CY	0.0	0.1	0.5	0.6	0.4	0.7
						CMCG	0.2	1.5	2.9	0.4	0.4	2.8
						CYMB	0.1	0.1	0.4	0.1	0.2	0.7
						CRMB	0.1	0.2	0.1	2.9	2.8	2.8
						CHMFL	0.9	1.7	1.4	0.3	0.3	0.7
						CHMFR	0.7	0.8	1.4	0.1	0.0	1.6
						CHMFLminusR						0.1

Table 3. Overall percentage of good CFD predictions by aerodynamic coefficient.

All cases		
Coef.	OVERFLOW	FUN3D
CA	100%	85%
CN	11%	18%
CY	91%	68%
CMCG	40%	32%
CYMB	57%	76%
CRMB	91%	85%
CHMFL	47%	31%
CHMFR	47%	59%

Looking a bit deeper at the results, the breakdown of good predictions by aerodynamic coefficient is given in Table 3. The objective of the current study was to determine the ability of CFD to accurately predict the aerodynamic effectiveness of control surfaces. In this context, the CFD predictions were not very accurate. CN, CMCG and CYMB and the hinge-moment coefficients, CHMFL and CHMFR, are the best indicator of successful modeling of the effectiveness of the flap control surfaces. Table 3 indicates that predicting these coefficients was mediocre at best.

Table 4 shows how the accuracy of the CFD prediction varies with Mach number. In the table, all data points at the nominal Mach numbers shown are included with all the Reynolds numbers that were tested and predicted. The predictions at Mach 2.4 missed the measurements more frequently than those at either Mach 3.5 or 4.6. This is consistent with the results from the inflow conditions at the three nominal Mach numbers. The vortex wake from the T-rail was much more pronounced at Mach 2.4 than at Mach 3.5 and 4.6 which indicates that the predictions either miss the location of the wake or do not predict the strength of the vortices in the wake. The comparisons in Table 4 also indicate that the predictions at Mach 4.6 are somewhat less accurate than at Mach 3.5, though still comparing with the wind-tunnel data better than for Mach 2.4. The predictions are also score slightly lower for the largest flap deflections. Both outcomes may be due to poor simulation of the flow physics associated with the compression corner flow separation and reattachment. Significantly more analysis and post-test CFD will go toward understanding the source of the prediction misses.

Table 4. Percentage of good CFD predictions by Mach number.

Mach 2.4			Mach 3.5			Mach 4.6		
Coef.	OVERFLOW	FUN3D	Coef.	OVERFLOW	FUN3D	Coef.	OVERFLOW	FUN3D
CA	100%	56%	CA	100%	93%	CA	100%	91%
CN	0%	6%	CN	16%	40%	CN	13%	0%
CY	85%	50%	CY	95%	83%	CY	93%	57%
CMCG	31%	0%	CMCG	63%	43%	CMCG	20%	43%
CYMB	31%	67%	CYMB	74%	83%	CYMB	60%	70%
CRMB	85%	89%	CRMB	95%	87%	CRMB	93%	74%
CHMFL	31%	0%	CHMFL	58%	47%	CHMFL	47%	35%
CHMFR	8%	33%	CHMFR	53%	70%	CHMFR	73%	61%

Table 5 shows the breakdown of good CFD predictions by flap configuration. There is no obvious difference in the accuracy of the predictions for configurations 1 through 4, however, the FUN3D predictions for configuration 13 do appear to be less accurate than for the other configurations shown. The OVERFLOW computations have not been completed yet for this configuration. This is notable in that the other configurations have either zero or positive flap deflections (trailing edge down) which either have a smooth transition from the body or form a forward-facing ramp. A forward-facing ramp can cause a separation bubble which is the flow feature that was the focus of this evaluation - whether the CFD simulations accurately model the flow on deflected control surfaces and the resulting changes in forces and moments.

Table 5. Percentage of good CFD predictions by flap configuration.

Config. 1 $\delta FL = \delta FR = 0^\circ$			Config. 2 $\delta FL = \delta FR = 20^\circ$			Config. 3 $\delta FL = 30^\circ \delta FR = 10^\circ$		
Coef.	OF	FUN3D	Coef.	OF	FUN3D	Coef.	OF	FUN3D
CA	100%	89%	CA	100%	92%	CA	100%	94%
CN	13%	17%	CN	0%	8%	CN	23%	19%
CY	100%	67%	CY	100%	77%	CY	77%	69%
CMCG	38%	33%	CMCG	45%	62%	CMCG	46%	31%
CYMB	63%	78%	CYMB	82%	92%	CYMB	38%	56%
CRMB	81%	56%	CRMB	100%	100%	CRMB	100%	100%
CHMFL	81%	39%	CHMFL	45%	54%	CHMFL	31%	38%
CHMFR	69%	61%	CHMFR	27%	46%	CHMFR	46%	75%

Config. 4 $\delta FL = \delta FR = 35^\circ$			Config. 13 $\delta FL = \delta FR = -35^\circ$		
Coef.	OF	FUN3D	Coef.	OF	FUN3D
CA	100%	87%	CA		33%
CN	0%	20%	CN		33%
CY	86%	60%	CY		56%
CMCG	29%	7%	CMCG		33%
CYMB	43%	73%	CYMB		78%
CRMB	86%	73%	CRMB		100%
CHMFL	0%	0%	CHMFL		22%
CHMFR	29%	33%	CHMFR		78%

C. Flap Asymmetry

The aerodynamic coefficient labeled CHMFLminusR in Table 2 is the difference between the measured flap hinge moment coefficients on the left and right-hand flaps from the experiment. The value in the adjacent cell is the average difference for the three angles of attack. The difference in coefficient is also shown as a multiple of the 1σ experimental hinge-moment coefficient uncertainty and when it exceeds 2, the cell is shaded. This is an indication for configurations with symmetric flap deflections and with 0° sideslip, like these two cases, that something is causing unexpected asymmetric flap loadings. These cases generally showed poorer prediction accuracy than cases showing more symmetric flap loadings and occur more often at Mach 2.4 than at Mach 3.5 and even less often at Mach 4.6.

After a careful check of the model geometry and the model support system, we were able to rule out asymmetric flap deflections on the model and potential offsets in the model support yaw settings. This left asymmetric flow in the test section as a potential culprit. Acquiring wind-tunnel data with the model moved laterally 4 inches showed a change in the flap asymmetry for symmetric flap deflections. Yawing the model from its normal centerline location

at a constant angle of attack also produced odd flap asymmetry rather than the expected slightly anti-symmetric loadings.

The CFD simulations of the empty test section [7] showed a vortex pair in the center of the test section. The source of the vortex wake is a T-shaped guide rail that is part of the sliding nozzle block mechanism used to set the nozzle throat for the desired test-section Mach number. In the simulations, the T-rail wake was strongest at Mach 2.4 and very much weaker at Mach 3.5 and 4.6 and was relatively insensitive to Reynolds number. Figure 14 shows the computed flow distributions at the beginning of the tests section ($X = 0$ inches) for Mach 2.4, 3.5, and 4.6.

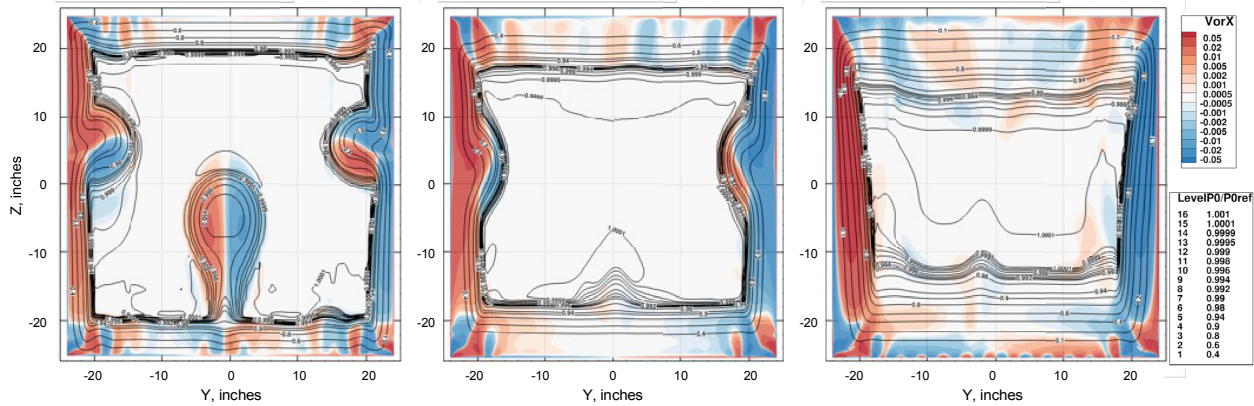


Fig. 14 Computed X-vorticity (color contours) and pitot pressure normalized by the reference total pressure (contour lines) at the start of the test section. OVERFLOW solutions for (a) $M = 2.4$, $Re = 3$ M/ft, (b) $M = 3.5$, $Re = 2$ M/ft, and (c) $M = 4.6$, $Re = 3$ M/ft.

Figure 15 shows the effect of moving the model from the test-section centerline laterally 4 inches at two different test conditions. At Mach 3.48 (Fig. 15a) the flap loads are relatively symmetric, up to about 65° angle of attack, with the model on the centerline but very asymmetric when moved off center by 4 inches. While not technically out of the realm of agreement given the measurement uncertainty, the repeatability is generally much better than the measurement uncertainty and the two data sets were acquired nearly back-to-back. The asymmetry at Mach 3.48 may indicate that the T-rail wake is still present at that tunnel speed. This is also one of the few examples of somewhat non-linear behavior of the CobraMRV mode, further adding to the suspicion about vortical flow at Mach 3.5. At Mach 4.57 the flap loads are slightly asymmetric, but neither the lateral position nor angle of attack has a significant effect on the magnitude of the asymmetry. The difference in hinge-moment coefficients is also small enough to not be statistically significant given the measurement uncertainty.

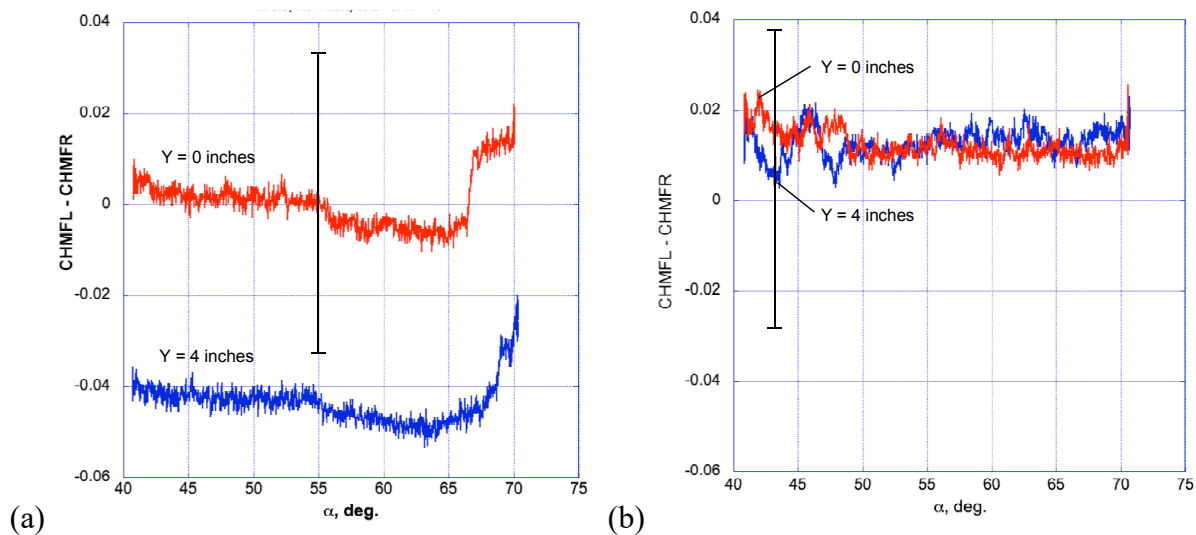


Fig. 15 Effect of lateral position of model in test section on the flap symmetry for symmetry flap deflections, $\delta F_L = \delta F_R = 20^\circ$. (a) $M = 3.48$, $Re = 1$ M/ft, $\beta = 0^\circ$. (b) $M = 4.57$, $Re = 2.5$ M/ft, $\beta = 0^\circ$.

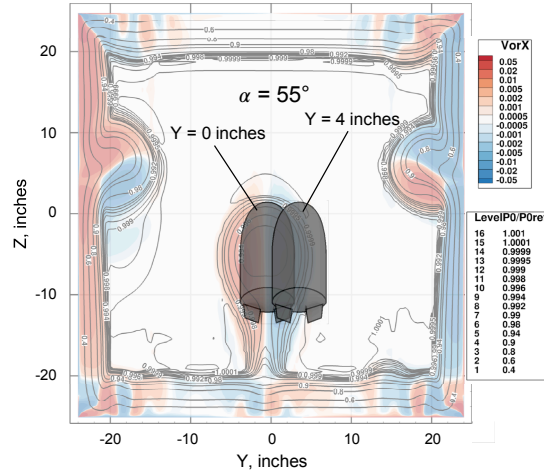


Fig. 16 Image of model in the test section superimposed on contours of X-vorticity (color) and total pressure (lines) at the start of the test section from an empty test section OVERFLOW prediction at Mach 2.4, Re 3 M/ft.

Figure 16 shows a graphic of the model in the test section superimposed on an OVERFLOW predicted empty-tunnel vorticity contour plot ($M = 2.4$, $Re = 3$ M/ft). In this case the prediction shows the T-rail wake located slightly to the left and below the center of the test section. Given these two positions of the model relative to the t-rail wake, one would expect the flap loads have different levels of asymmetry.

D. Pressure Distributions

Further evidence of the asymmetric flap loads comes from the measured pressure distribution compared with the predictions. Figure 16 shows two comparisons of the pressures on the model surface measured using PSP and generated by the two CFD codes. At $X/L = 0.31$, the measured (PSP) and predicted (FUN3D and OVERFLOW) pressure distributions around the model perimeter agree quite well. At about $1/3^{\text{rd}}$ of the flap chord, however, there are differences that illustrate the flap asymmetry in the experimental data and some interesting differences between the two simulations.

The measured pressures clearly indicate significantly different loads being generated by the two flaps while the predicted flap loads are symmetric with FUN3D predicting slightly higher flap loads than OVERFLOW. The PSP data has occasional dropouts, especially on the flaps that are caused by poor visibility from the camera, inadequate lighting, or missing paint on the model, but the data is good over most of the surface. The overall impression from this comparison, as well as at other test conditions and different model configurations, is that the experimental environment is different from the simulations, and the two simulated environments may also be slightly different from each other.

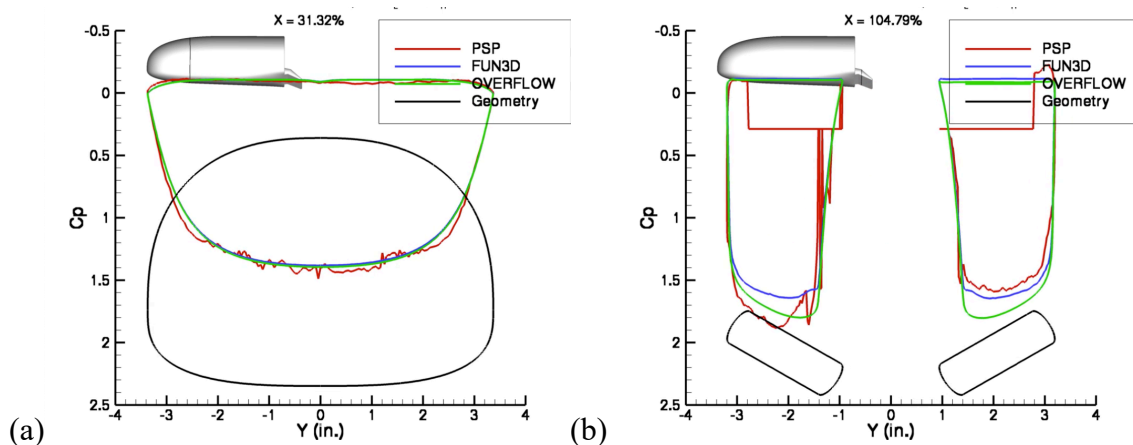


Fig. 16 Comparisons of predicted and measured pressure distributions for 35° symmetric flap deflections at $\alpha = 55^\circ$, $M = 3.48$, $Re = 1$ M/ft. (a) $X/L = 0.31$, (b) $X/L = 1.05$.

To illustrate the second point about the test-section environments, Figure 17 shows the inflow boundary conditions used in the OVERFLOW and FUN3D computations. They were generated independently and compared with the available wind-tunnel measurements [7]. The contour plots are indeed slightly different with the t-rail vortex differing slightly, both in location and strength. The differences in the predicted flap loadings from the two CFD codes is at plausible. The symmetry of the predicted T-rail wake position in both codes also falls in line with the pressure coefficient plots in Figure 16.

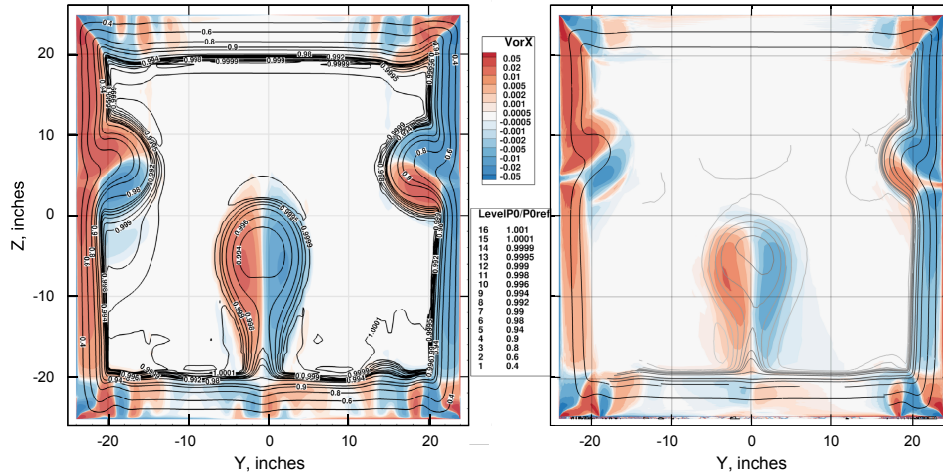


Fig. 17 Inflow BC generated by the two CFD codes (a) OVERFLOW and (b) FUN3D. X = 0 inches, Mach 2.4, Re = 3 M/ft.

An important note is that during this work and the empty test section flow characterization [1, 7], a very simple fairing was developed that, at least in the CFD simulations, eliminated the T-rail vortex wake. Therefore, a major recommendation from the study is to retrofit the nozzle-block T-rail with the fairing to reduce the uncertainty in the data generated in the tunnel.

VII. Cost Comparison

An important part of the CFD Evaluation Project is to compare the costs of running a wind-tunnel test and running an equivalent set of CFD predictions. This requires all participants to keep track of the time spent in various activities associated with both the wind-tunnel test and the CFD predictions. The goal was to account for all costs and to generate a cost estimate for doing just the CFD evaluation pieces of the experiment and CFD efforts and the cost for generating the data for building the CobraMRV aerodynamic database.

Table 6 shows the way the costs were collected for the wind-tunnel test. This is straightforward accounting when applied to the total cost of the testing. Splitting it into the two different tests was also mostly straightforward. This was done by assigning percentages of each cost line to each type of test, that is the amount of a particular cost item that would typically be borne by each of the two test types. The table shows the estimated percentages. Knowing the total cost for each of the cost items, the cost of each type was then estimated. The test cost for the evaluation test was chosen as the quantity to normalize the costs by so it has a cost of 1. This accounting led to an estimate for a database test for the CobraMRV model costing 65% of the cost of the evaluation test.

Table 7 shows how the CFD costs were broken down. Each of the CFD team members kept track/estimated the number of hours spent in the labor categories shown. Breaking the labor out into these categories will allow a subsequent analysis of the time spent and where process improvements will have the most benefit. For the purposes of this study, the total labor hours were the most important. The labor and computer usage (SBU, Standard Billing Units on the NASA NAS system) for the preparation, guideline development, job management, data visualization and uncertainty quantification.

Table 6. Estimated relative cost of the wind-tunnel experiment. The estimated cost of the evaluation test is used as the baseline with the overall cost of the wind-tunnel test and the estimated cost of a database test shown as multiples of the baseline.

			Rate		FY20
			4' SSWT hourly rate		\$
			Avg. labor rate		\$
Item	Labor or WT hours	Procurement	Total Cos, %	Evaluation Cost, %	Database Cost, %
Geometry Development			100%	100%	100%
Model design & fab management			100%	100%	100%
Model fabrication			100%	100%	100%
Test lead and other "customer" labor			100%	100%	70%
Special Instrumentation:					
	PSP		100%	100%	100%
	DGV		100%	100%	
	IR		100%		
	Hinge-moment gages		100%	100%	100%
WT occupancy (Total)			100%		
WT power (Total)			100%		
WT occupancy (Evaluation)				66%	
WT power (Evaluation)					71%
WT occupancy (Database)					54%
WT power (Database)					46%
Total			1.13		
			Evaluation	1.00	
				Database	0.65

Table 7. Estimated relative cost of the wind-tunnel experiment. The estimated cost of the evaluation test is used as the baseline with the overall cost of the wind-tunnel test and the estimated cost of a database test shown as multiples of the evaluation test cost.

										FY 20 SBU cost		\$
										FY 20 average burdened labor, \$K		\$
Name	Total hours	CAD/Geom Prep	Simulation Guidelines - Best Practices	Meshing	Database Framework Development & Scripting	CFD Job Management	Data-review & Reporting	Visualization & Understanding Data (CFD&WT)	Uncertainty Quantification	SBU (2020-21)	NAS Queue Time per job (hrs)	Average Job Run Time (SBU)
Totals:												
Total Evaluation CFD Cost						0.39						
Total Database CFD Cost						1.12						

There was no CFD-based database developed so that cost was estimated. An attempt was made to account for all of the pre-computation labor and computer time, allowing for reduced CAD/Geometry preparation, data visualization, and CFD job management hours per CFD case run (assumed economy of scale). The number of solutions required for a database is significantly higher than the total run for the CFD evaluation. The assumption for this well-behaved vehicle configuration is that the 115 runs performed in this study for the database with 10 angles of attack each would be a minimum requirement. Obviously more data was acquired during the database portion of the test as it was performed as continuous sweeps in angle of attack at a given Mach number, Reynolds number, and yaw angle – approximately 1,100 points per sweep. Reducing that to 10 points for an untested configuration would not be prudent even if it is sufficient in this case. This estimate puts the cost of this bare-bones database definition using CFD at approximately 10% higher than an equivalent (with much more data) wind-tunnel test.

For the vehicle used for this study, this difference in cost is probably negligible. Most vehicles have more control surfaces than the CobraMRV, and the aerodynamic behavior can be much more non-linear. Either of these would result in a significantly larger number of data points required of the CFD and increase the cost of the CFD relative to a wind-tunnel test.

Of course, most database development processes involve both CFD and wind-tunnel testing, which has proven to be a very efficient process that provides valuable information unavailable without doing both. A more representative combination of the two would make a more realistic baseline with which to compare with a CFD-only process. The comparison presented here should therefore be interpreted in that light.

VIII. Conclusion

The overall goal of the CFD Evaluation project was to see if CFD could replace the capabilities of the Unitary Plan Wind Tunnel at NASA's Langley Research Center. This would require that the CFD predictions of any test in the high-speed leg of the wind tunnel reliably match the wind-tunnel measurements to within the experimental measurement uncertainty. That would represent a minimum requirement for CFD to not require wind-tunnel data for verification when applied to new configurations. It is also the only metric we have for the current study. The goal is to ensure that we have a path to accurate prediction of flight behavior and of new flow physics discoveries. This specific study looked at the ability of CFD to accurately predict the control-surface effectiveness on a vehicle of interest, that is the change in aerodynamics with changes in control-surface deflection angles. The results indicate that the CFD employed did not reliably predict these changes for the CobraMRV configuration through the Mach number range 2.4 to 4.6. Some of the difficulty in obtaining accurate predictions is likely due to the inability to accurately model the flow in the wind tunnel itself. Our experimental measurements of the flap hinge moments indicates that the vortex wake from the T-rail is not centered in the test section while the CFD simulations show those vortices basically on the lateral center and somewhat below the vertical center of the test section. Previous CFD simulations also showed that the T-rail vortex wake diminished significantly at Mach 3.5 and above while there was still some asymmetry in the flap loads, indicating that the wake may persist at higher Mach numbers.

References

- [1] Ross, J.C., Rhode, M. N., Falman, B. E., Edquist, K. T., Schoenenberger, M., Witte, D. W., Brauckmann, G. J., Kleb, B. L., West, T. K., and Alter, S. J., "Evaluation of CFD as a Surrogate for Wind-Tunnel Testing for Mach 2.4 to 4.6 - Project Overview", AIAA Aviation Conference, August 2021.
- [2] Garcia, J. A., Brown, J. L., Kinney D. J., Bowles, J. V., Huynh L. C., Jiang X. J., Lau E., Dupzyk, I. C., "Co-Optimization of Mid Lift to Drag Vehicle Concepts for Mars Atmospheric Entry," 10th AIAA/ASME Thermophysics Conference, 2010.
- [3] Denison, M. F., et al, "Pre-Test CFD Predictions of CobraMRV Control Surface Effectiveness at the NASA Langley Unitary Plan Wind Tunnel," AIAA Aviation 21 Conference, August 2021.
- [4] Derlaga, J. M., Jackson, C. W., and Buning, P. G., "Recent Progress in OVERFLOW Convergence Improvements," AIAA paper 2020-1045, AIAA SciTech Forum, 6-10 January 2020, Orlando FL.
- [5] Biedron, R. T., et al, "FUN3D Manual: 13.7," NASA TM-20205010139, Langley Research Center, November 2020.
- [6] Jackson, Jr., C. M., Corlett, W. A., and Monta, W. J., "Description and Calibration of the Langley Unitary Plan Wind Tunnel," NASA Technical Paper NASA TP-1905, NASA Langley Research Center, Langley Research Center, Hampton, VA, 1981.
- [7] Childs, R. E., Stremel, P. M., Hawke, V. M., Garcia, J. A., Kleb, W. L., Hunter, C., Parikh, P., Patel, M., Alter, S., and Salari, K., "Flow Characterization of the NASA Langley Unitary Plan Wind Tunnel, Test Section 2: Computational Results," AIAA Aviation 21 Conference, August 2021.
- [8] Burns, R. A., Fahringer, T. W., and Danehy, P. M., "Velocity Measurements Across an Oblique Shock Using Pulse-Burst Cross-Correlation DGV," AIAA Scitech 2021 Forum, January 2021, Virtual Event.
- [9] "Standard: Assessment of Experimental Uncertainty with Application to Wind Tunnel Testing" (AIAA S-071A-1999), American Institute of Aeronautics and Astronautics, 1999.
- [10] Rhode, M. N. and Oberkampf, W. L., "Estimation of Uncertainties for a Model Validation Experiment in a Wind Tunnel," Journal of Spacecraft and Rockets, Vol. 54, No. 1, January-February 2017, pp. 155-168.
- [11] Baurle, R. A. and Axdahl, E. L., "Uncertainty Quantification of CFD Data Generated for a Model Scramjet Isolator Flowfield," JANAF...